

SIMULATIONS OF THE SYMBIOTIC RECURRENT NOVA V407 CYG. I. ACCRETION AND SHOCK EVOLUTIONS

Kuo-Chuan Pan (潘國全)¹, Paul M. Ricker², and Ronald E. Taam^{3,4}

¹Physik Department, Universität Basel, Klingelbergstrasse 82, CH-4056 Basel, Switzerland;

kuo-chuan.pan@unibas.ch

²Department of Astronomy, University of Illinois at Urbana–Champaign, 1002 West Green
Street, Urbana, IL 61801, USA; pmricker@illinois.edu

³Department of Physics and Astronomy, Northwestern University, 2145 Sheridan Road,
Evanston, IL 60208, USA; r-taam@northwestern.edu

⁴Academia Sinica Institute of Astronomy and Astrophysics, P.O. Box 23-141, Taipei 10617,
Taiwan; taam@asiaa.sinica.edu.tw

Received _____; accepted _____

ABSTRACT

The shock interaction and evolution of nova ejecta with a wind from a red giant star in a symbiotic binary system are investigated via three-dimensional hydrodynamics simulations. We specifically model the March 2010 outburst of the symbiotic recurrent nova V407 Cygni from the quiescent phase to its eruption phase. The circumstellar density enhancement due to wind-white dwarf interaction is studied in detail. It is found that the density-enhancement efficiency depends on the ratio of the orbital speed to the red giant wind speed. Unlike another recurrent nova, RS Ophiuchi, we do not observe a strong disk-like density enhancement, but instead observe an aspherical density distribution with $\sim 20\%$ higher density in the equatorial plane than at the poles. To model the 2010 outburst, we consider several physical parameters, including the red giant mass loss rate, nova eruption energy, and ejecta mass. A detailed study of the shock interaction and evolution reveals that the interaction of shocks with the red giant wind generates strong Rayleigh-Taylor instabilities. In addition, the presence of the companion and circumstellar density enhancement greatly alter the shock evolution during the nova phase. The ejecta speed after sweeping out most of the circumstellar medium decreases to $\sim 100 - 300 \text{ km s}^{-1}$, depending on model, which is consistent with the observed extended redward emission in [N II] lines in April 2011.

Subject headings: hydrodynamics — methods: numerical, — novae: general — stars:individual: V407 Cygni

1. INTRODUCTION

The symbiotic recurrent nova (SyRN) V407 Cyg consists of a white dwarf (WD) and a Mira-type red giant (RG, Munari et al. 1990). In March 2010, the gamma-ray emission from its outburst was detected by *Fermi*-LAT (Large Area Telescope, Atwood et al. 2009), showing the first evidence for a gamma-ray nova (Abdo et al. 2010). Another gamma-ray SyRN, V745 Sco, was also detected by *Fermi*-LAT in February 2014 (Cheung et al. 2014). Since the RGs in symbiotic binaries could produce a high-density circumstellar medium (CSM) through their stellar wind, gamma-ray emission in SyRNe could originate in high-energy particle acceleration that happens when blast waves pass through the high-density CSM (Abdo et al. 2010; Martin & Dubus 2013).

Recently, classical novae (CNe) have also been classified as a new type of gamma-ray source (Ackermann et al. 2014). However, the lack of a high-density CSM in CNe cannot explain the origin of gamma-ray emission as in SyRNe, requiring a new mechanism for gamma-ray CNe. Chomiuk et al. (2014) studied the high-resolution radio maps of the gamma-ray CN V959 Mon, proposing that the fast binary motion in CNe could shape the nova ejecta by transferring its angular momentum. Therefore, high-energy particles could be accelerated at the interface between equatorial and polar regions.

Since particle acceleration in CNe and SyRNe is highly associated with shock propagation in their nova eruptions, these new discoveries motivate us to study the shock evolution in nova systems. Additionally, SyRNe have long been considered as Type Ia supernova (SN Ia) progenitors (Hachisu & Kato 2001; Kato & Hachisu 2012), although the nature of the progenitor systems of SNe Ia remains uncertain (Maoz et al. 2014). However, evidence of interaction between SN Ia ejecta with a CSM has been found in some SNe Ia in late-type spiral galaxies (Patat et al. 2007; Dilday et al. 2012; Silverman et al. 2013), suggesting that at least some SNe Ia could originate in symbiotic binaries.

The gamma-ray emission from the 2010 outburst of V407 Cyg has been studied by Martin & Dubus (2013) through a semi-analytical study of diffusive shock acceleration and non-thermal emission in V407 Cyg. They found that the observed gamma-ray light curve could be fitted by requiring a circumbinary density enhancement (CDE) around the WD. Multi-dimensional hydrodynamics simulations by Orlando & Drake (2012) further support the need for a CDE around the WD. They simulated a blast wave passing through a dense CSM in V407 Cyg including a sophisticated treatment of thermal conduction and radiative cooling (Orlando & Drake 2012), finding that the observed X-ray light curves could be reproduced if a CDE exists around the WD. However, they do not include the asymmetric effect of binary motion, and the distribution of CDE is artificially imposed in their simulations without modeling the WD-wind interaction in the quiescent phase.

On the other hand, Walder et al. (2008) performed three-dimensional hydrodynamics simulations of another SyRN, RS Oph, from the quiescent phase to a nova eruption. In their simulations, they found a disk-like CDE concentrated in the orbital plane, and their shock evolution is consistent with the observations of the 2006 nova outburst (Sokoloski et al. 2006; Bode et al. 2006). Although some similarity between RS Oph and V407 Cyg has been found in their eruptions’ spectra (Munari et al. 2011; Shore et al. 2011), the physical parameters of the binary systems are quite different (Drozd et al. 2013), especially for their orbital periods (separations). The orbital period in RS Oph is much shorter ($P_{\text{orb}} \sim 1.25$ yr) than in V407 Cyg ($P_{\text{orb}} \sim 43$ yr). Therefore, the amount and distribution of density enhancement could be different in these two systems.

In this paper, we investigate the evolution of the SyRN V407 Cyg from the quiescent phase to a nova eruption. In the next section, we review and summarize some observational facts about the binary system of V407 Cyg and its previous outbursts. The numerical methods and the initial setup are presented in Section 3. Our simulation results with

different red giant wind loss rates and nova eruption parameters are reported and discussed in Section 4. In the final section, we summarize our results and conclude.

2. OBSERVATIONS OF V407 CYG

As mentioned in the above section, the SyRN V407 Cyg consists of a massive WD and a Mira-type M6 III RG (Munari et al. 1990). The Mira-type RG has a pulsation period of 763 day (Kolotilov et al. 2003). From the dust obscuration and the long-term optical light curve, an orbital period of ~ 43 yr was inferred by Munari et al. (1990), corresponding to an orbital separation of 16 AU for a $1M_{\odot}$ RG and a $1.2M_{\odot}$ WD. The distance of V407 Cyg is still unclear. Some distance estimates using the period-luminosity relation give a range from 1.7 kpc (Kolotilov et al. 2003) to 2.7 kpc (Munari et al. 1990). However, Chomiuk et al. (2012) suggest a possible distance $\gtrsim 3.0$ kpc using the interstellar Na I D absorption lines, since the period-luminosity relation is not well established for the long pulsation period of V407 Cyg (Whitelock et al. 2008) (see a more detailed argument in Chomiuk et al. 2012).

V407 Cyg has been monitored in the optical for more than seven decades. Three nova eruptions were reported in 1936, 1998, and 2010 (Schaefer 2010), although some undetected eruptions could have happened in this interval. The March 2010 eruption is the most interesting due to the use of modern astronomical instrumentation and the detection of gamma-rays. From the measurement of an H_{α} emission line-width, an ejecta mass $M_{\text{ej}} \sim 10^{-6}M_{\odot}$, eruption energy $E_{\text{ej}} \sim 10^{44}$ ergs, and ejecta speed $v_{\text{ej}} \sim 3,200 \pm 345$ km s $^{-1}$ could be estimated (Abdo et al. 2010; Schwarz et al. 2011). An ejecta mass of $M_{\text{ej}} \sim 10^{-6}M_{\odot}$ could also reproduce the observed velocity evolution, but may underestimate the RG mass loss rate (Chomiuk et al. 2012).

In general, the observed mass loss rate \dot{M}_{wind} of a Mira giant spans a wide range, varying from $\sim 10^{-8} M_{\odot} \text{ yr}^{-1}$ to $\sim 10^{-4} M_{\odot} \text{ yr}^{-1}$ with an average $\langle \dot{M}_{\text{wind}} \rangle \sim 6 \times 10^{-7} M_{\odot} \text{ yr}^{-1}$ (Knapp & Morris 1985). The radio light curve from the 2010 outburst of V407 Cyg suggests a mass loss rate $\dot{M}_{\text{wind}} \sim 2 \times 10^{-6} M_{\odot} \text{ yr}^{-1}$ (for $v_{\text{wind}} = 10 \text{ km s}^{-1}$ and $d = 3 \text{ kpc}$; Chomiuk et al. 2012), but this mass loss rate is one order of magnitude higher than the estimated value from the X-ray light curve ($\dot{M}_{\text{wind}} \sim 10^{-8} - 10^{-7} M_{\odot} \text{ yr}^{-1}$, Nelson et al. 2012; Martin & Dubus 2013). To obtain better agreement between the X-ray and radio estimates, a binary separation wider than 16 AU may be required (Chomiuk et al. 2012).

The wind speed of a giant star correlates with the star’s luminosity (De Beck et al. 2010; Politano & Taam 2011). Taking account of the observed luminosity $L \sim 10^4 L_{\odot}$ (Munari et al. 2011) and the uncertainty of the distance of V407 Cyg, a RG wind speed of $10 - 20 \text{ km s}^{-1}$ can be estimated. In addition, a wind speed of $\sim 10 \text{ km s}^{-1}$ could be also estimated from the optical P Cygni line profiles (Abdo et al. 2010). However, a higher wind speed of 30 km s^{-1} is estimated from the equivalent width of the Na I D lines in the quiescent phase (Tatarnikova et al. 2003) and in the eruption phase (Shore et al. 2011; Nelson et al. 2012).

3. NUMERICAL METHODS

3.1. Simulation Code

The simulation code used in this study is FLASH¹ version 4 (Fryxell et al. 2000; Dubey et al. 2008; Lee 2013). FLASH is a grid-based, parallel, multidimensional hydrodynamics code based on block-structured adaptive mesh refinement (AMR). The split piecewise parabolic method (PPM) solver (Colella & Woodward 1984) is used to solve for the motion

¹<http://flash.uchicago.edu>

of compressible fluids. We use active particle clouds to represent the WD and the core of the RG companion. Particle clouds are utilized instead of single particles to avoid the force anisotropy problem in cloud-in-cell interpolation (Ricker & Taam 2008; Pan et al. 2012). Gravitational forces between particle clouds and gas and self-gravity are solved using a multigrid Poisson solver (Ricker 2008). Nuclear burning is ignored in our simulations, since it takes place in the envelope of the white dwarf, which is not resolved. We also assume that magnetic fields do not affect the shock evolution.

3.2. Initial Setup

To model V407 Cyg and its 2010 eruption, we consider a three-dimensional (3D) simulation box with a size of $400 \text{ AU} \times 400 \text{ AU} \times 400 \text{ AU}$. Initially, a $1M_{\odot}$ RG is located at the center (origin) of the simulation box, and a $1.2M_{\odot}$ WD is located on the positive x -axis with a binary separation of 16 AU, corresponding to an orbital period of about 43 yr. The orbital plane is set on the $x-y$ plane and the direction of angular momentum is set to be the positive z -axis. Particle clouds representing the WD and the RG have a radius of 10^{13} cm , which is slightly larger than three smallest zone spacings ($\Delta x_{\min} = 2.93 \times 10^{12} \text{ cm}$). We use 9 levels of refinement based on the magnitudes of the second derivatives of gas density and pressure. Each AMR block contains 8^3 zones in the 3D simulation box, corresponding to an effective uniform resolution of 2048^3 . To save computation time, we reduce the maximum AMR level based on the distance to the center of mass, giving an effective resolution of $\Delta x^i \sim 0.61 \times d$ at the i th level of AMR, where d is the distance to the center of mass of the WD-RG binary. The highest resolution region contains the central 65 AU and the first forced AMR decrement occurs at $d \sim 32 \text{ AU}$. The second AMR decrement occurs at $d \sim 63 \text{ AU}$, the third at $d \sim 127 \text{ AU}$, and so on. Outflow boundary conditions for fluids and isolated boundary conditions for the Poisson solver are used.

We assume the RG has a radius of 2.2 AU, a constant wind speed $v_{\text{wind}} = 20 \text{ km s}^{-1}$ in the co-rotating frame, and a constant mass loss rate \dot{M}_{wind} . Therefore, the initial gas density ρ is distributed using Equation 1:

$$\rho(r) = \frac{\dot{M}_{\text{wind}}}{4\pi r^2 v_{\text{wind}}} = 1.12 \times 10^{-14} \left(\frac{\dot{M}_{\text{wind}}}{10^{-6} \text{ M}_{\odot} \text{ yr}^{-1}} \right) \left(\frac{v_{\text{wind}}}{20 \text{ km s}^{-1}} \right)^{-1} \left(\frac{r}{1 \text{ AU}} \right)^{-2} \text{ g cm}^{-3}, \quad (1)$$

where r is the distance to the RG. We assume a gamma-law equation of state with $\gamma = 1.1$ and wind temperature $T_{\text{wind}} = 7,000 \text{ K}$ to mimic the thermodynamic behavior of gas based on photoionization models of symbiotic binary systems (Nussbaumer & Vogel 1987; Nussbaumer & Walder 1993).

We perform quiescent-phase simulations up to $\sim 2.0 - 2.5$ orbital periods, since the density distribution becomes quasi-steady in the co-rotating frame after about 1.5 orbital periods. During the quiescent phase, we reset the RG wind using Equation 1 for the region with $r < 5 \text{ AU}$ to maintain the RG wind.

To model a SyRN eruption, we artificially impose a Sedov-like explosion on the location of the WD. The eruption has an ejecta mass M_{ej} , eruption energy E_{ej} , and averaged ejecta speed v_{ej} . To avoid grid effects, the eruption covers a small spherical region with a radius equal to fifteen smallest zone spacings (Pan et al. 2012). Within the erupting region, a uniform density distribution and linear velocity profile in radius are used. We assume the kinetic energy is three-fourths of the total eruption energy (Dohm-Palmer & Jones 1996). The mass and kinetic energy of the CDE within the exploding region and the orbital speed of the WD are added to the eruption. Once the SyRN eruption is imposed, we reduce the resetting radius for the RG wind to the radius of the RG, and assume a completely absorbing surface on the RG. In reality, this assumption is not precisely correct, and a reverse shock should be generated when the ejecta reach the surface of the RG. We ignore these effects since the purpose of the paper is not to focus on the response of the RG, but on the global shock evolution.

4. RESULTS AND DISCUSSION

We perform runs with several different sets of values for the RG wind and SyRN eruption parameters, such as \dot{M}_{wind} , E_{ej} , and M_{ej} (see Table 1), and present our simulation results in this section. In the first subsection, the evolution of wind focused by the WD during the quiescent phase is described. The asymmetry due to WD-wind interaction is investigated as well. In Section 4.2, we study the shock evolution dependence on different RG wind loss rates and different eruption energies and ejecta masses.

4.1. Quiescent Phase

We perform two quiescent-phase simulations by varying the mass loss rate from $\dot{M}_{\text{wind}} = 10^{-6} M_{\odot} \text{ yr}^{-1}$ (model M6) to $\dot{M}_{\text{wind}} = 10^{-7} M_{\odot} \text{ yr}^{-1}$ (model M7; see Table: 1) to study the effects on the CDE. The quiescent phase evolution of both models is qualitatively the same, but the gas density distributions scale with their mass loss rates. In this subsection, we take model M6 as the reference simulation and describe the quiescent-phase evolution in detail.

Figure 1 demonstrates a typical evolution of the gas density in the orbital plane during the quiescent phase (model M6). Since the initial wind density distribution (see Equation 1) neglects the binary interaction, a turbulent and hot spiral arm quickly forms when the RG wind interacts with the WD. This turbulent spiral arm takes about an orbital period ($\sim 40 \text{ yr}$) to reach a quasi-steady large-scale state in the co-rotating frame. We also show the corresponding gas temperature distribution in Figure 2.

The WD gravitationally deflects matter in its vicinity. Figure 3 shows the mass within control surfaces for different radii for our models M6 and M7. It is clear that the enclosed mass increases for the first few years and then reaches stability after about 10 yr. Since the

RG wind speed is higher than the orbital speed of the WD, the WD experiences a strong wind which limits the amount of mass enclosed within the control surface. Therefore, we observe no significant wind-capture disk around the WD as reported by Walder et al. (2008), since the wind speed relative to the orbital speed is much higher than that in RS Oph. However, we do observe a small, elongated, disk-shaped structure around the WD with a size about 5 AU (See Figure 4). This result is consistent with the fast simulation case ($v_{\text{wind}} = 60 \text{ km s}^{-1}$) of RS Oph in Walder et al. (2010), since the orbital speed of RS Oph ($v_{\text{orb}} \sim 15 \text{ km s}^{-1}$) is much faster than that in V407 Cyg ($v_{\text{orb}} \sim 5 \text{ km s}^{-1}$), giving a similar orbital to wind speed ratio of $v_{\text{orb}}/v_{\text{wind}} \sim 1/4$. We note, however, that the enclosed mass is not gravitationally bound to the WD. As the WD ($R_{\text{WD}} \sim 4 \times 10^8 \text{ cm}$) is not resolved in our simulations, we cannot determine the mass accreted by the WD.

For $r < 3 - 5 \text{ AU}$, the enclosed mass is enhanced up to $\sim 3 - 4$ times, independent of the radius of the control surface and the mass loss rate. Qualitatively, the models M6 and M7 behave similarly, but the density is one order of magnitude higher in model M6 than in model M7. In addition, a short-period oscillation ($P \sim 2 \text{ yr}$) in the enclosed mass is also observed. This prompt oscillation reflects the dynamical timescale around the WD due to the interaction between the colliding RG wind and the turbulent flow behind the WD.

The CDE, including the spiral arm, is concentrated in the equatorial plane. However, the CDE does not form a thin disk, but instead shows a mild anisotropy. This is due to a relatively large pressure scale height ($H_p \sim c_s/\Omega$) in V407 Cyg, where Ω is the angular velocity. Figures 5 and 6 show the gas column density and gas density-weighted temperature distribution as viewed from within the orbital plane. The density enhancement is only about $\sim 20 - 40\%$, but the temperature can be heated to $\sim 20,000 \text{ K}$. The opening angle of the spiral arm is about $\sim 30 - 50$ degrees. As described above, when the RG wind collides with the WD, some gas periodically puffs out from the WD and forms the ring-like density

distribution in Figure 5.

Figure 7 and 8 show the angle-averaged density profiles of models M6 and M7 within surface of cones having different inclination angles. Each density profile is averaged from 180 uniformly distributed radial rays in a given inclination angle and each radial ray is sampled from the surface of the RG to the boundary of the simulation box. From the upper panels, the averaged density profiles still follow the $1/r^2$ distribution, but with about 20 – 40% variation for different inclination angles. It is also clear that the density distribution at about $r < 70 - 80$ AU is highly concentrated in the region with $\theta < 60^\circ$. Beyond this scale, the asymmetry is small and only affected at high inclination angles.

We have also performed a low-resolution run by reducing the maximum AMR level to 8 and enlarging the finest zone size to $\Delta x_{\min} = 5.86 \times 10^{12}$ cm, corresponding to a factor of 2 larger than the standard resolution. In this low-resolution run, the spiral arm qualitatively looks the same as in the standard run, and the averaged density distribution looks the same as well, but the turbulence is slightly suppressed due to a higher numerical viscosity. The enclosed mass within the same control surface ($r < 5R_c$) is about 20% higher than the standard run.

It should be noted that in our model we assume a constant RG wind speed during the whole quiescent-phase simulation. However, in reality the RG wind is driven by radiation pressure on dust formed above the stellar surface during the Mira giant’s pulsation (Willson 2000). The wind acceleration zone could extend to about $5 - 10R_{\text{RG}}$ (Bowen 1988), which is comparable to the binary separation in V407 Cyg. Therefore, the wind speed could be less than what we have assumed when it collides with the WD, implying that our estimate of the CDE could be low.

4.2. Eruption Phase

After running for two orbital periods in the quiescent-phase simulations, we impose a nova eruption on the WD. We perform two eruption simulations with two different eruption energies ($E = 1.2 \times 10^{43}$ erg and $E = 1.2 \times 10^{44}$ erg) and ejecta masses ($M_{\text{ej}} = 10^{-7} M_{\odot}$ and $M_{\text{ej}} = 10^{-6} M_{\odot}$) for each quiescent-phase simulation. Since we assume that the averaged ejecta speed is $\langle v_{\text{ej}} \rangle = 3,000$ km/sec and the kinetic energy ($E_{\text{kin}} = \frac{1}{2} M_{\text{ej}} \langle v_{\text{ej}} \rangle^2$) is three-fourths of the total eruption energy at the onset of eruption (Dohm-Palmer & Jones 1996), a higher eruption energy implies a larger ejecta mass in that eruption, and vice versa. In total, we have four different sets of 3D eruption simulations as described in Table 1. In Section 4.2.1, we adopt model M6E44 as the reference simulation to describe the overall evolution in the eruption phase. We also discuss the shock evolution in all our models in Section 4.2.2.

4.2.1. A Qualitative Description of the Evolution after the Nova Eruption

Figure 9 shows a typical gas density distribution for V407 Cyg in the orbital plane after a nova eruption. In this case (model M6E44 in Table 1), the mass loss rate of the RG wind is $M_{\text{wind}} = 10^{-6} M_{\odot} \text{ yr}^{-1}$, the ejecta mass is $M_{\text{ej}} = 10^{-6} M_{\odot}$, and the eruption energy is $E = 1.2 \times 10^{44}$ erg. At about one week after the eruption, the forward shock sweeps out the RG wind and the spiral arm (label A), and forms a reverse shock propagating backward to the WD (label B). The two shocks are separated by a contact discontinuity. At ~ 15 days, the forward shock reaches the RG. The propagation of the forward shock and the reverse shock can be seen in Figure 10. Note that although we assume the RG completely absorbs the forward shock when it reaches the surface of the RG, it does not affect the propagation of the reverse shock from the eruption.

Subsequently, Rayleigh-Taylor instabilities quickly develop (label C in Figure 9). After the forward shock passing through the RG, the RG wind and the CDE are shocked and heated (label D). These hot and dense plasma could be the source of X-ray emission (Orlando & Drake 2012). The self-interaction of Rayleigh-Taylor bubbles and the interaction of the forward shock with the spiral arm produce additional reverse shocks as well. When these reverse shocks collide with each other, filament-like shocks form at about 70 days after the eruption (label E).

After 70 days, the forward shock has slowed down because of the positive density gradient toward the RG, forming a heart-shaped structure. Once the forward shock has passed the RG, a high-density tail at the back side of the RG is formed (label F). Within the forward shock, several filaments are formed and destroyed repeatedly due to the interaction of the reverse shocks (label G). The turbulent spiral arm is completely destroyed by the forward shock. The corresponding gas temperature distribution is shown in Figure 11. It is clear that the temperature distribution is highly asymmetric due to the RG wind interaction and Rayleigh-Taylor instabilities. High Mach number shocks are associated with the forward shock, starting from $M \gtrsim 10$ in the first week and then decreasing with time. Once the Rayleigh-Taylor instabilities have developed, the Mach number decreases to $M \sim 5$ and is maintained at this level for several months.

A 3D volume rendering of the gas density distribution right before and after ($t = 137$ day) a nova eruption is shown in Figure 12. The orange color shows the location of the forward shock. Several filaments and Rayleigh-Taylor bubbles can also be seen.

In Figure 13 and 14, we show the gas column density and gas density-weighted temperature distribution in the $r - z$ plane (edge-on view), to demonstrate the aspherical evolution of the shock radius due to the CDE. As we described in the previous subsection, the CDE makes the density $\sim 20\%$ asymmetric at different inclination angles. Therefore,

although the ejecta speed is much higher than the orbital speed and the gravitational binding energy of the CDE is much less than the eruption energy, the ejecta speed greatly decreases in the equatorial direction due to the CDE and the RG wind. The ratio of the shock radius in the poleward and equatorial directions is about $1.2 - 1.7$, depending on the location of the RG.

Orlando & Drake (2012) have performed simulations of the 2010 eruption of V407 Cyg with an artificial CDE. They found that the observed X-ray emission could be reproduced if there is a CDE around the WD, but is not required if the outburst energy and ejecta mass are near the upper end of the range for these characteristics for classical novae, which would be extreme for SyRN. Comparing the results of their best-fitting simulation model with CDE, E44.3-NW7-CDE6.3-L40 with our results for model M7E44, we find that their forward shock expands more spherically and about twice as fast as that found here. Orlando & Drake (2012) found that most X-ray emission originates from the shocked CSM. The observed X-ray emission reaches a maximum at around 40 days after the eruption and declines after 50 days (Shore et al. 2011). This corresponds to the time when the RG wind and the CDE are heated by the shock in our simulations (see label D in Figure 9). A lower shock expansion velocity in our simulations in comparison with Orlando & Drake (2012) may affect the shape of simulated X-ray lightcurve. However, we note that the initial averaged ejecta velocity $\langle v_{\text{ej}} \rangle \sim 9,000 \text{ km s}^{-1}$ in Orlando & Drake (2012) is probably too high based on recent observations (Abdo et al. 2010).

Since the nova eruption completely destroys the CDE and creates a cavity that contains the binary system at the end of the simulation, the subsequent circumstellar density distribution will need several years to decades to reestablish the original wind profile (Equation 1). The last recorded nova eruption of V407 Cyg prior to the 2010 eruption was in 1998. Assuming that there were no undetected eruptions between the 1998

and 2010 eruptions and the RG wind has a constant wind speed of 20 km s^{-1} , the newly developed wind profile could only reach to about $\sim 50 \text{ AU}$ in distance. Therefore, our initial wind profile (Equation 1) may not be valid at large distances, which may affect our shock evolution at late times ($t > 3 \text{ months}$ for Model M6E44).

If we reduce the resolution by a factor of 2 as we did in the quiescent-phase simulations, we see no notable difference in the shock locations within $r < 150 \text{ AU}$, but the Rayleigh-Taylor instabilities are less obvious due to a higher numerical viscosity. The filaments produced by the interaction of reverse shocks are slightly less clear than in the standard run, but overall the evolution does not change significantly.

4.2.2. Shock Evolutions

Understanding the shock evolution in nova eruptions is crucial, since the high-energy charged particles required for the nonthermal gamma-ray and radio emission are likely produced in the shock front. Overall, the simulation results for the shock positions and evolution during the eruption phase runs are qualitatively similar, but quantitatively very different. Therefore, in this subsection we describe the shock evolution of our four eruption simulations in detail.

Figure 15 to Figure 18 show the shock evolution in all the eruption simulations. At the very beginning of a nova eruption ($t < 1 \text{ week}$), the eruption is nearly free-expanding and the shock location is nearly spherically symmetric. Since the kinetic energy is the dominant form of energy at that time and we assume the initial averaged ejecta speed is the same in different runs, the shock radius evolution is similar in all cases. However, later on, when the ejecta sweep up enough mass, the forward shock slows down due to momentum conservation. The decline rate depends on the eruption energy and the RG mass loss rate.

For instance, if we lower the eruption energy or the ejecta mass by an order of magnitude (case M6E43), the shock location would be slowed down by a factor of ~ 2 at $t \sim 200$ days (Figure 16). Similarly, with the same eruption energy, the shock would propagate much faster if the surrounding CDE were less dense (Figure 17).

Nelson et al. (2012) and Martin & Dubus (2013) have described a simple semi-analytical model for the shock evolution by comparing the circumstellar mass distribution with the ejecta mass plus swept mass using momentum conservation. In their model, the density distribution is described by a 1D wind profile (Equation 1) plus a CDE. The CDE is assumed to be a gaussian distribution which can be described by

$$\rho_{\text{CDE}}(r, \theta) = \rho_{0,\text{CDE}} \exp \left(- \left(\frac{r \sin \theta}{b} \right)^2 - \left(\frac{r \cos \theta}{l} \right)^2 \right), \quad (2)$$

where $\rho_{0,\text{CDE}}$, l , and b are density and length scale parameters. We perform similar calculations by comparing the shock location of our 3D hydrodynamic simulations with the semi-analytical model described by Martin & Dubus (2013).

To find the most suitable sets of parameter values, we apply two constraints. First, we assume the $\rho_{0,\text{CDE}}$ in model M6 is one order of magnitude higher than that in M7, i.e. $\rho_{0,\text{CDE}}(\text{M6})/\rho_{0,\text{CDE}}(\text{M7}) = 10$, based on the analysis from Figure 7 and 8. Second, we assume the length-scale parameters l and b are equal, since we do not observe significant asymmetry in the local density enhancement around the WD. By applying these two constraints, a best-fit set of parameter values is: for M7, $l = b = 20$ AU and $\rho_{0,\text{CDE}} = 8 \times 10^{-18}$ g cm $^{-3}$; and for M6, $l = b = 20$ AU and $\rho_{0,\text{CDE}} = 8 \times 10^{-17}$ g cm $^{-3}$. The best-fit shock evolution is shown using the red dotted lines in Figures 15 - 18.

The best fit model in Orlando & Drake (2012), which can reproduce the X-ray lightcurve, corresponds to their model E44.3-NW7-CDE6.3-L40. It is characterized by an ejecta mass of $2 \times 10^{-7} M_{\odot}$, eruption energy $E = 2 \times 10^{44}$ erg, $\rho_{0,\text{CDE}} \sim 3 \times 10^{-18}$ g cm $^{-3}$, and $b = l = 40$ AU. The CDE in this model is comparable to, in order of magnitude, with

our model M7, but is less concentrated. However, as described above, the ejecta speed in Orlando & Drake (2012) is much faster than adopted in our work.

Figure 19 shows the averaged forward shock evolution in the orbital plane and poleward regions of all considered models in Table 1. The shock radius evolution can be characterized as $r_{\text{sh}} \propto t^\alpha$, where α is an evolution stage-dependent constant. Depending on the model, α is around $0.5 - 0.8$ during the first week. At the beginning, the ejecta are nearly spherically symmetric, but the angle-averaged forward shock evolves slightly faster in the orbital plane than in the poleward direction due to the orbital motion. Later on, the shock interaction with the RG reduces the angle-averaged shock speed in the orbital plane, making α decrease a little for $10 < t < 100$ days. After about 100 days, the forward shock is far beyond the RG, and α increases again. This behavior is consistent with the result in Walder et al. (2008), but for a different time scale due to differences in binary parameters. Furthermore, if we increase the RG mass loss rate (from model M7E44 to M6E44 or model M7E43 to M6E43) or decrease the eruption energy (model M6E43 to M6E44 or model M7E43 to M7E44), α becomes lower.

The angle-averaged shock speed decreases greatly due to the sweeping out of the RG wind. Starting from a value of $v_{\text{ej}} \sim 3,000 \text{ km s}^{-1}$ at the onset of the nova eruption, the average shock speed in the radial direction drops to $v_{\text{ej}} \sim 100 - 300 \text{ km s}^{-1}$ after about a year. The evolution of shock speed can be characterized as another power-law relation with an index of $-\frac{1}{3} \sim -\frac{1}{2}$ (Figure 19). The speed evolution in Figure 19 is roughly consistent with the spherically symmetric simulation of Moore & Bildsten (2012). In their simulation, a better treatment of the radiative cooling during shock expansion is implemented, but only in 1D. Our shock speed is also comparable with the observed ejecta speed (star symbols in Figure 19) of $\sim 2760 \text{ km s}^{-1}$ on day +2.3 and $\sim 200 \text{ km s}^{-1}$ on day +196 from the FWHM of the broad component of $H\alpha$ (Munari et al. 2011). By fitting the simulated ejecta speed

with observations, the best-matched models are M6E44 and M7E43. Furthermore, the 2011 April observation also shows that the maximum velocity is $\lesssim 300 \text{ km s}^{-1}$ (Shore et al. 2011), which is also consistent with our simulations. The decrement of nova ejecta speed with the existence of a CDE in our simulations is also consistent with the observed ejecta velocity decrement in RS Oph.

5. CONCLUSIONS

We have investigated the symbiotic recurrent nova V407 Cyg from the quiescent phase to a nova eruption via three-dimensional hydrodynamical simulations. In quiescent-phase simulations, we examined two different mass loss rates of the Mira-type RG. We studied the CDE produced due to the wind-WD interaction in V407 Cyg. It is found that the induced spiral accretion wake in V407 Cyg is more turbulent and the CDE is less efficient than found in RS Oph (Walder et al. 2008) due to a relatively high wind-to-orbital speed ratio. In addition, we observe no significant wind-captured disk around the WD as reported by Walder et al. (2008) in RS Oph, though the angle-averaged radial density profile in the equatorial plane is about 20% higher than that in the poleward direction.

The shock evolution in the eruption phase also is studied. It is found that the forward shock location is highly dependent on the inclination angle, nova eruption energy, and circumstellar density distribution. The forward and reverse shock interactions with the RG wind and CDE are also crucial factors in the overall evolution. In addition, the shock radius evolution can be characterized by a power law, $r_{\text{sh}} \propto t^\alpha$, where α is about 0.5 – 1.0, depending on model and evolution stage. Our model M6E44 ($M_{\text{ej}} = 10^{-6} M_\odot$ and $E_{\text{ej}} = 1.2 \times 10^{44} \text{ erg}$) and model M7E43 ($M_{\text{ej}} = 10^{-7} M_\odot$ and $E_{\text{ej}} = 1.2 \times 10^{43} \text{ erg}$) show good agreement with the observed ejecta speed from Munari et al. (2011). The shock evolution in the presence of CDE in our simulations is similar to what has been observed in

V407 Cyg and RS Oph.

Further work in this series of papers will include investigation of thermal and non-thermal emission in V407 Cyg and other symbiotic nova systems at different wavelengths, in particular in gamma-ray, X-ray, and radio. Similar analysis can be applied to other RNe and CNe as well.

KCP would like to thank continuous support from F.-K. Thielemann. This work was supported by the European Research Council (ERC) grant FISH, by PASC High Performance Computing Grant DIAPHANE, and by the Theoretical Institute for Advanced Research in Astrophysics (TIARA) in the Academia Sinica Institute of Astronomy and Astrophysics (ASIAA). PMR and RET acknowledge support by the NSF Division of Astronomical Sciences under AAG 14-13367. FLASH was developed largely by the DOE-supported ASC/Alliances Center for Astrophysical Thermonuclear Flashes at the University of Chicago. Analysis and visualization of simulation data were completed using the analysis toolkit `yt` (Turk et al. 2011).

REFERENCES

- Abdo, A. A., Ackermann, M., Ajello, M., et al. 2010, *Science*, 329, 817
- Ackermann, M., Ajello, M., Albert, A., et al. 2014, *Science*, 345, 554
- Atwood, W. B., Abdo, A. A., Ackermann, M., et al. 2009, *ApJ*, 697, 1071
- Bode, M. F., O’Brien, T. J., Osborne, J. P., et al. 2006, *ApJ*, 652, 629
- Bowen, G. H. 1988, *ApJ*, 329, 299
- Chomiuk, L., Krauss, M. I., Rupen, M. P., et al. 2012, *ApJ*, 761, 173
- Chomiuk, L., Linford, J. D., Yang, J., et al. 2014, *Nature*, 514, 339
- Cheung, C. C., Jean, P., & Shore, S. N. 2014, *The Astronomer’s Telegram*, 5879,
- Colella, P., & Woodward, P. R. 1984, *Journal of Computational Physics*, 54, 174
- De Beck, E., Decin, L., de Koter, A., et al. 2010, *A&A*, 523, AA18
- Dilday, B., Howell, D. A., Cenko, S. B., et al. 2012, *Science*, 337, 942
- Dohm-Palmer, R. C., & Jones, T. W. 1996, *ApJ*, 471, 279
- Drozd, K., Swierczynski, E., Ragan, E., & Buil, C. 2013, *Advances in Astronomy and Space Physics*, 3, #...75
- Dubey, A., Reid, L. B., & Fisher, R. 2008, *Physica Scripta Volume T*, 132, 014046
- Fryxell, B., Olson, K., Ricker, P., et al. 2000, *ApJS*, 131, 273
- Hachisu, I., & Kato, M. 2001, *ApJ*, 558, 323
- Kato, M., & Hachisu, I. 2012, *Bulletin of the Astronomical Society of India*, 40, 393

- Knapp, G. R., & Morris, M. 1985, *ApJ*, 292, 640
- Kolotilov, E. A., Shenavrin, V. I., Shugarov, S. Y., & Yudin, B. F. 2003, *Astronomy Reports*, 47, 777
- Lee, D. 2013, *Journal of Computational Physics*, 243, 269
- Martin, P., & Dubus, G. 2013, *A&A*, 551, A37
- Maoz, D., Mannucci, F., & Nelemans, G. 2014, *ARA&A*, 52, 107
- Moore, K., & Bildsten, L. 2012, *ApJ*, 761, 182
- Munari, U., Margoni, R., & Stagni, R. 1990, *MNRAS*, 242, 653
- Munari, U., Joshi, V. H., Ashok, N. M., et al. 2011, *MNRAS*, 410, L52
- Nelson, T., Donato, D., Mukai, K., Sokoloski, J., & Chomiuk, L. 2012, *ApJ*, 748, 43
- Nussbaumer, H., & Vogel, M. 1987, *A&A*, 182, 51
- Nussbaumer, H., & Walder, R. 1993, *A&A*, 278, 209
- Pan, K.-C., Ricker, P. M., & Taam, R. E. 2012, *ApJ*, 750, 151
- Patat, F., Chandra, P., Chevalier, R., et al. 2007, *Science*, 317, 924
- Patat, F., Chugai, N. N., Podsiadlowski, P., et al. 2011, *A&A*, 530, AA63
- Politano, M., & Taam, R. E. 2011, *ApJ*, 741, 5
- Ricker, P. M. 2008, *ApJS*, 176, 293
- Ricker, P. M., & Taam, R. E. 2008, *ApJ*, 672, L41
- Schaefer, B. E. 2010, *ApJS*, 187, 275

- Schwarz, G. J., Ness, J.-U., Osborne, J. P., et al. 2011, *ApJS*, 197, 31
- Shore, S. N., Wahlgren, G. M., Augusteijn, T., et al. 2011, *A&A*, 527, A98
- Silverman, J. M., Nugent, P. E., Gal-Yam, A., et al. 2013, *ApJS*, 207, 3
- Sokoloski, J. L., Luna, G. J. M., Mukai, K., & Kenyon, S. J. 2006, *Nature*, 442, 276
- Orlando, S., & Drake, J. J. 2012, *MNRAS*, 419, 2329
- Tatarnikova, A. A., Marrese, P. M., Munari, U., Tomov, T., & Yudin, B. F. 2003, *Astronomy Reports*, 47, 889
- Turk, M. J., Smith, B. D., Oishi, J. S., et al. 2011, *ApJS*, 192, 9
- Walder, R., Folini, D., & Shore, S. N. 2008, *A&A*, 484, L9
- Walder, R., Folini, D., Favre, J. M., & Shore, S. N. 2010, *Numerical Modeling of Space Plasma Flows*, *Astronom-2009*, 429, 173
- Willson, L. A. 2000, *ARA&A*, 38, 573
- Whitelock, P. A., Feast, M. W., & van Leeuwen, F. 2008, *MNRAS*, 386, 313

Table 1. Simulation Parameters

Abbreviation	\dot{M}_{wind}^a ($M_{\odot} \text{ yr}^{-1}$)	A^b (AU)	v_{wind}^c (km sec $^{-1}$)	T_{wind}^d (K)	E_{ej}^e (erg)	M_{ej}^f (M_{\odot})
Quiescent phase						
M6 [†]	10^{-6}	16	20	7,000	—	—
M7	10^{-7}	16	20	7,000	—	—
Eruption phase						
M6E43	10^{-6}	16	20	7,000	1.2×10^{43}	10^{-7}
M6E44 [†]	10^{-6}	16	20	7,000	1.2×10^{44}	10^{-6}
M7E43	10^{-7}	16	20	7,000	1.2×10^{43}	10^{-7}
M7E44	10^{-7}	16	20	7,000	1.2×10^{44}	10^{-6}

[†]Reference simulation

^aRG mass loss rate

^bBinary separation

^cRG wind speed

^dEffective wind temperature

^eEruption energy

^fEjecta mass

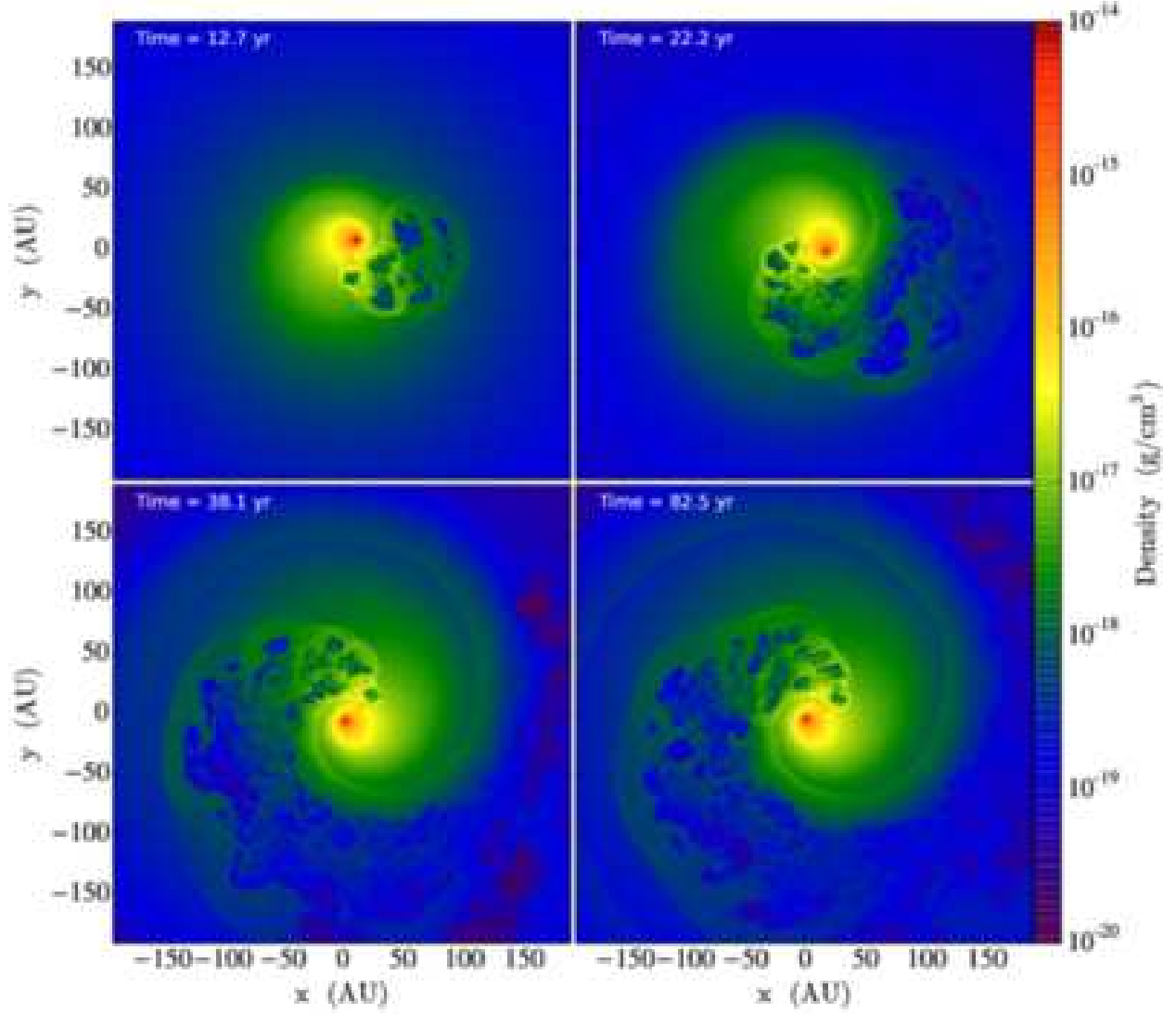


Fig. 1.— Gas density distribution in the orbital plane for model M6 at different labeled times. The color scale indicates the logarithm of the gas density in g cm^{-3} .

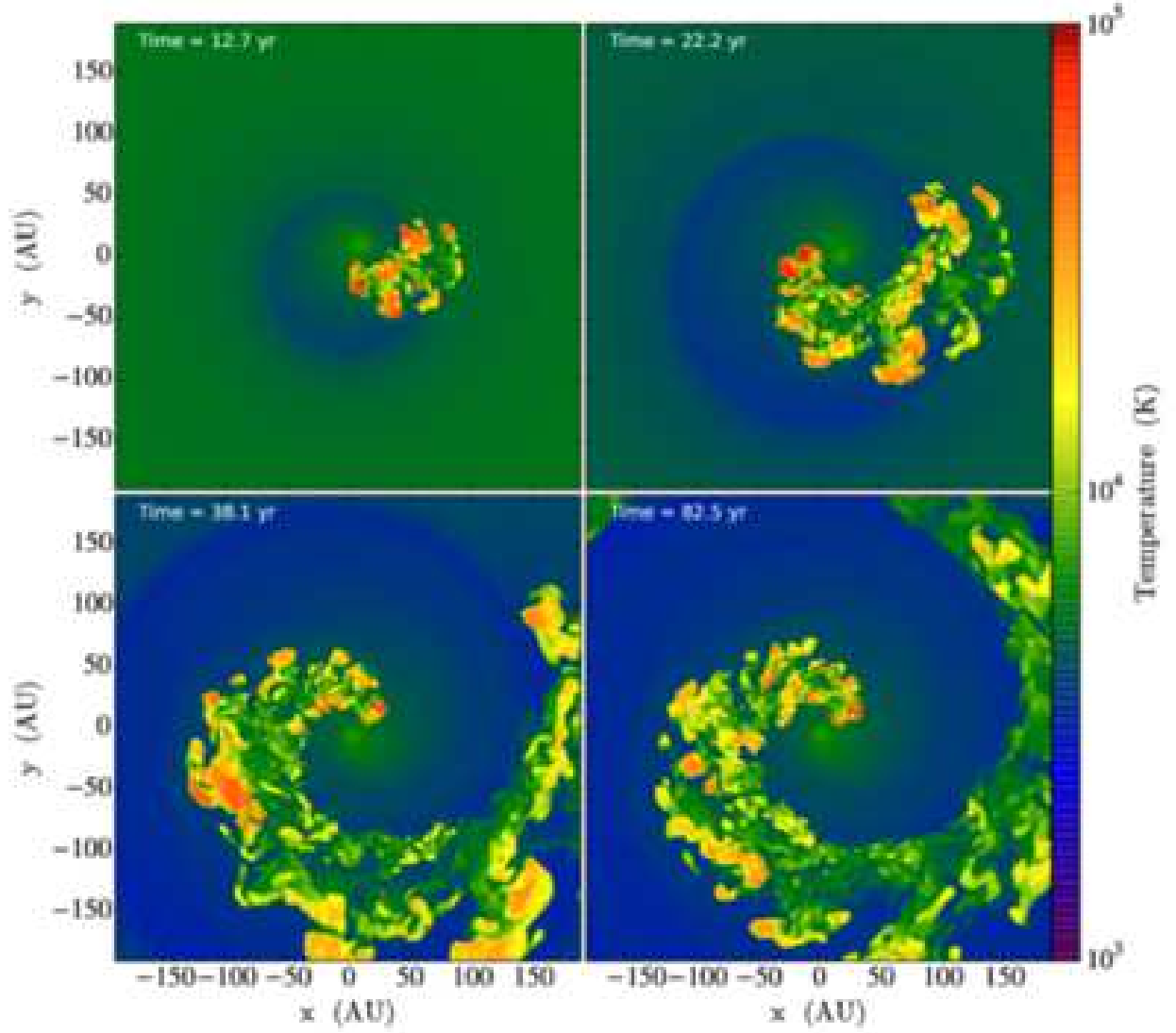


Fig. 2.— Gas temperature distribution in the orbital plane for model M6 at different labeled times. The color scale indicates the logarithm of the gas temperature in K .

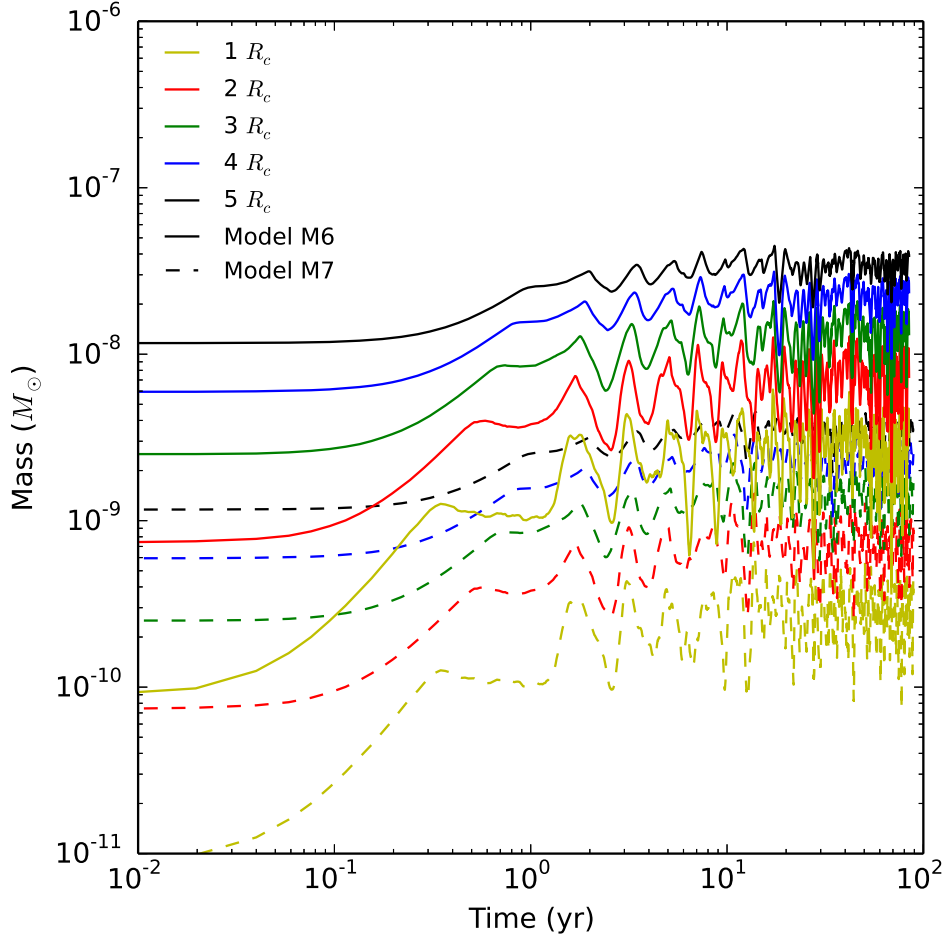


Fig. 3.— Mass in the vicinity of the WD companion as determined for spherical control surfaces of different radii ($R_c = 10^{13}$ cm) as a function of time during the quiescent phase. Different line styles indicate different mass loss rates of the RG wind (see Table 1).

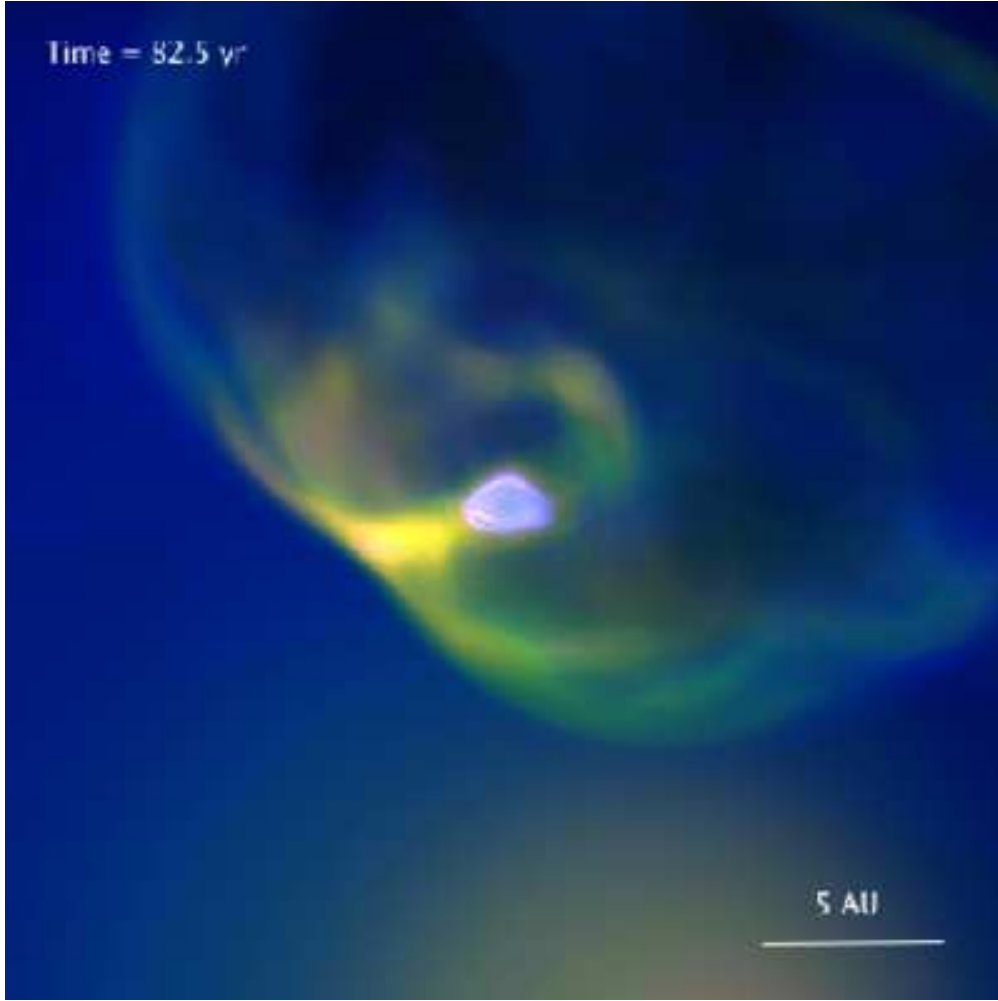


Fig. 4.— 3D volume rendering of gas density around the WD for model M6. The white region represents the disc-like accretion flow around the WD and the yellow region on the left indicates the colliding shock front from the RG wind. The RG cannot be seen in this figure, but the bright region at the bottom shows the location of the RG.

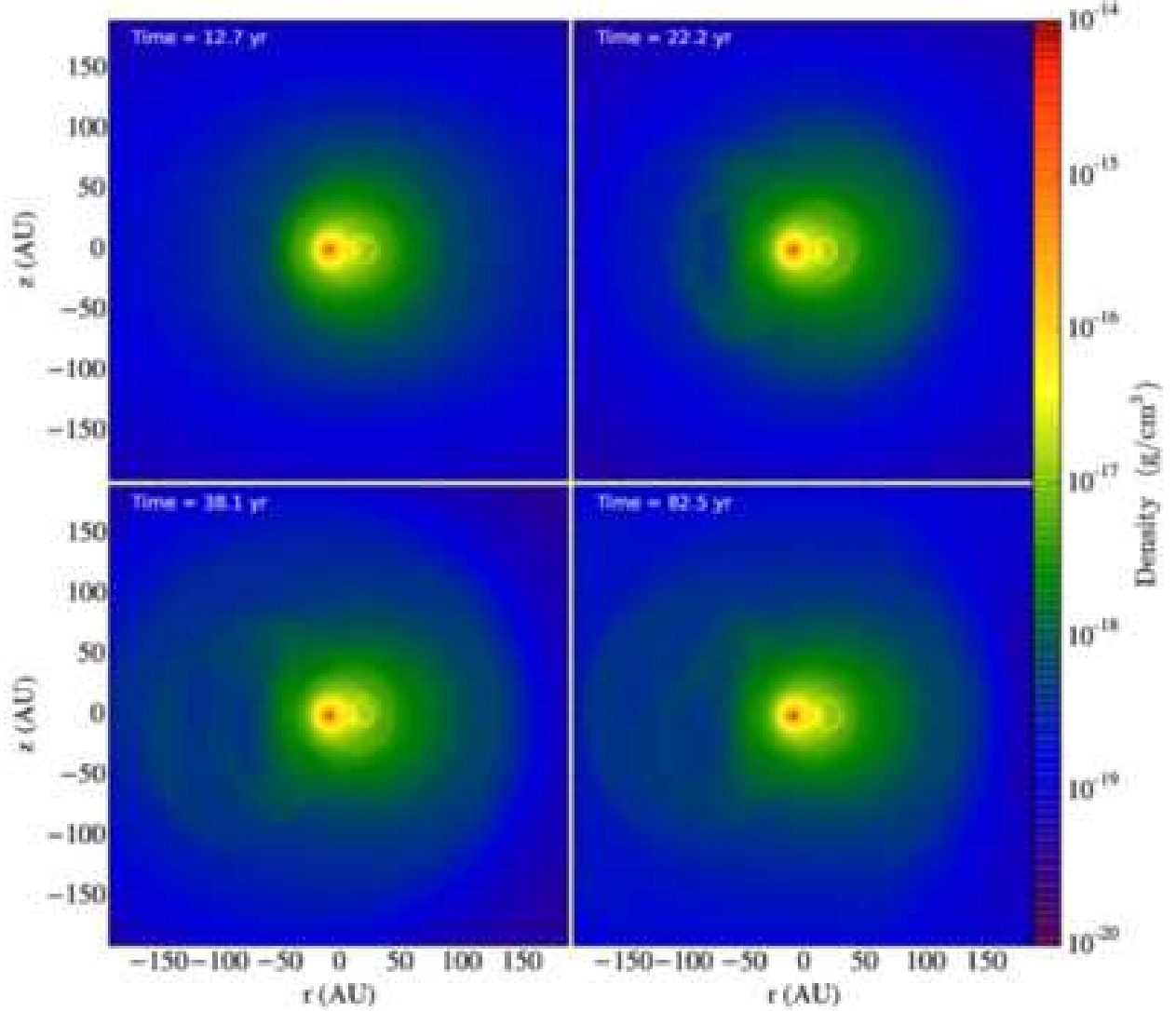


Fig. 5.— Gas density projection in the $r - z$ plane perpendicular to the orbital plane for model M6 at different labeled times, where the r -axis represents the axis passing through the RG and the WD. Note that the origin of the r -axis in this plot is at the center of mass, which is different from the simulation coordinate origin. In this figure, the RG is located on the left. The color scale indicates the logarithm of the gas density in g cm^{-3} .

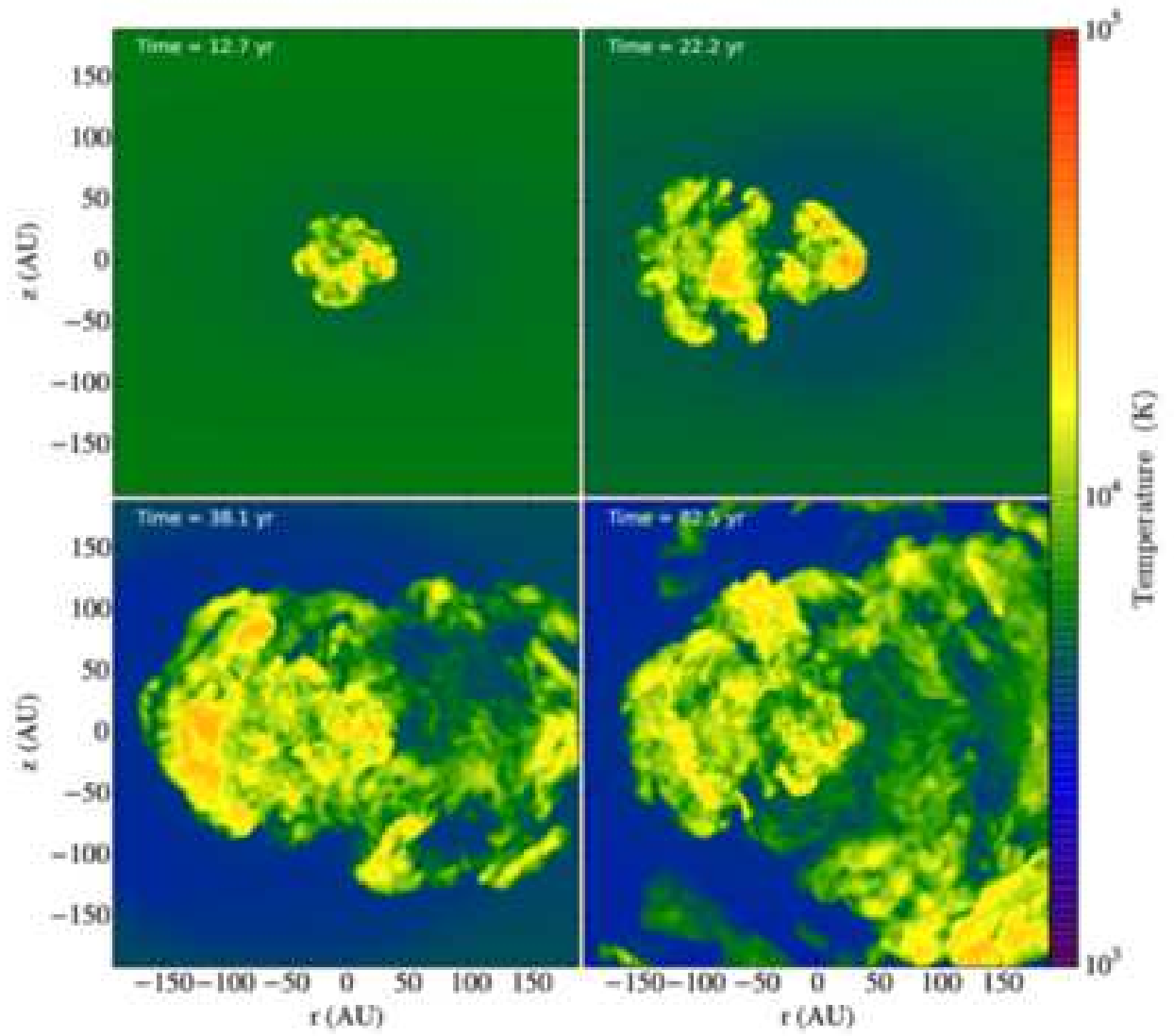


Fig. 6.— Similar to Figure 5 but for gas temperature.

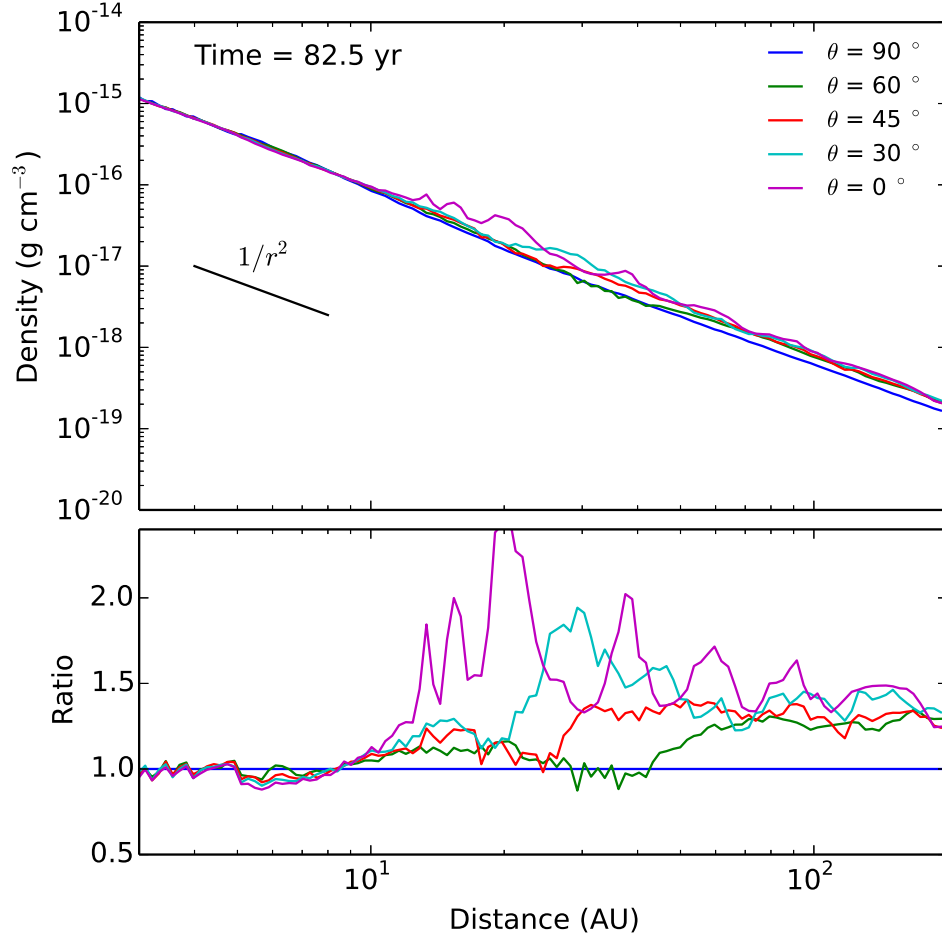


Fig. 7.— Top: Averaged density profile of model M6 with different inclination angles as a function of radius at 82.5 yr. Bottom: The ratio of the density at different inclination angles to that along the rotation axis.

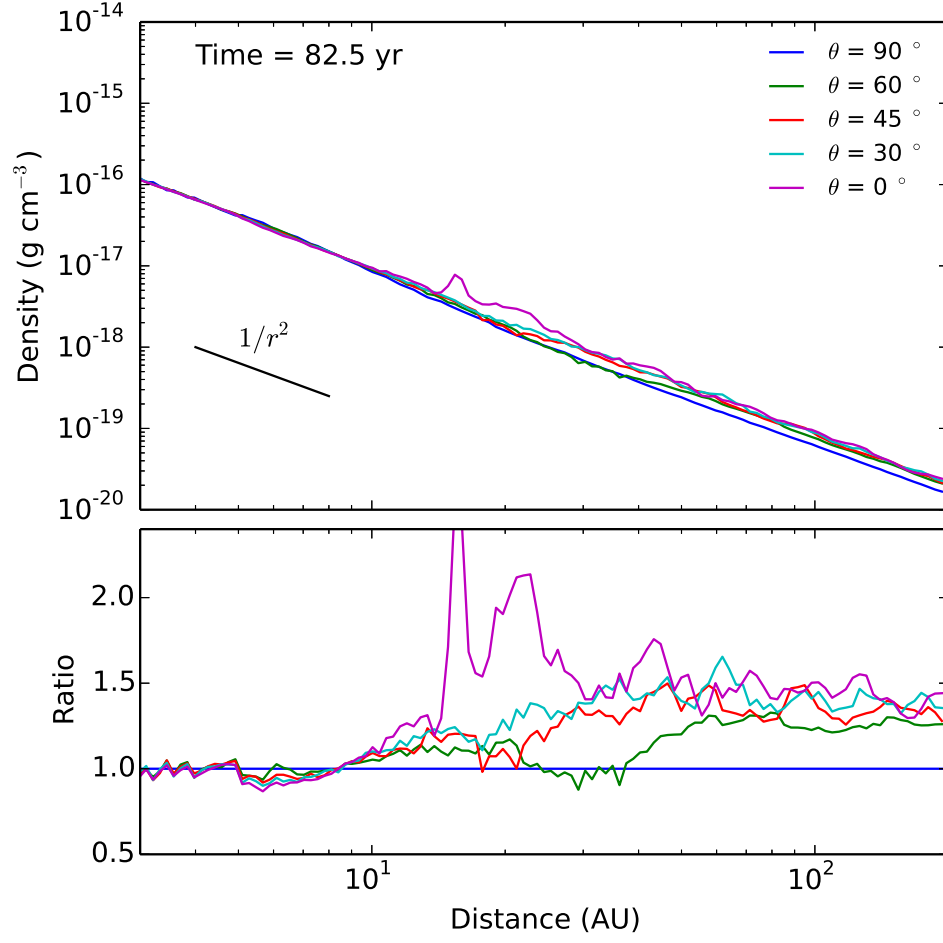


Fig. 8.— Similar to Figure 7 but for model M7.

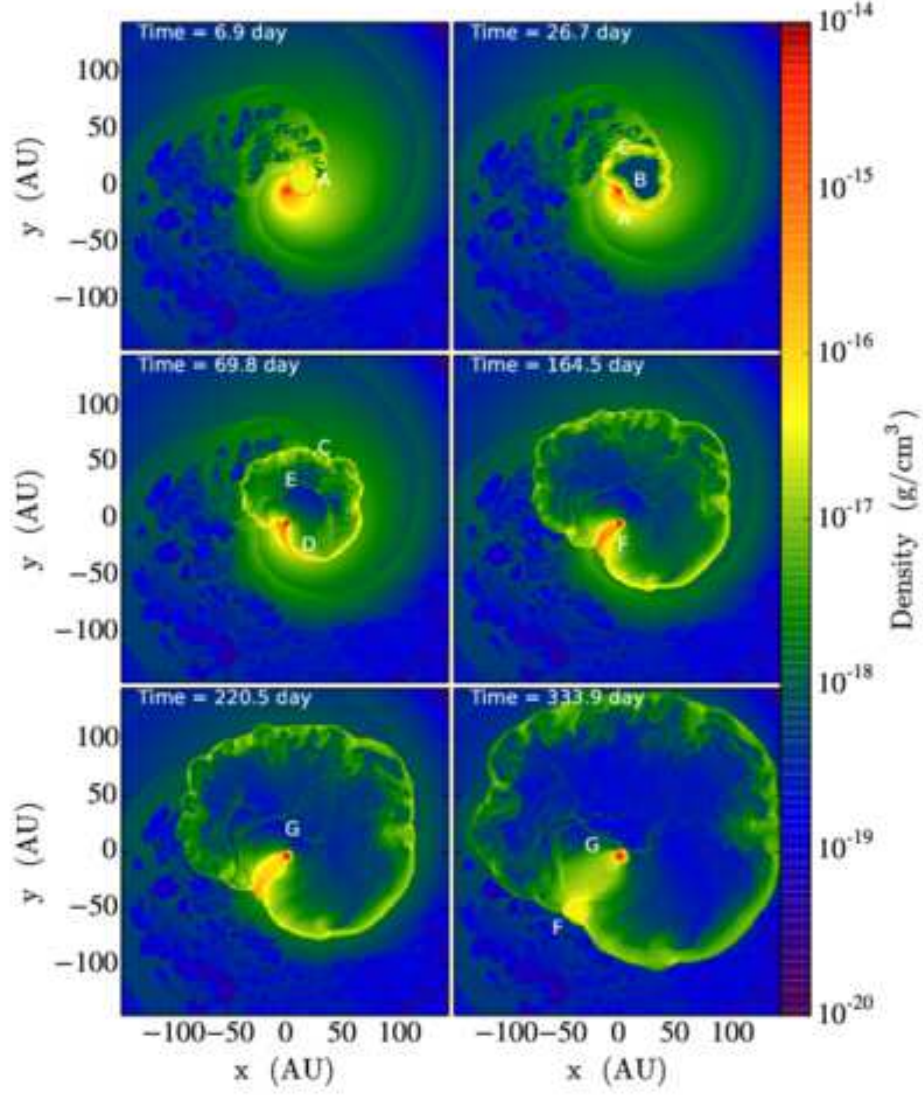


Fig. 9.— Similar to Figure 1 but for the eruption phase of model M6E44. The labeled times indicate the time after a nova eruption. Labels are important features that are described in Section 4.2.

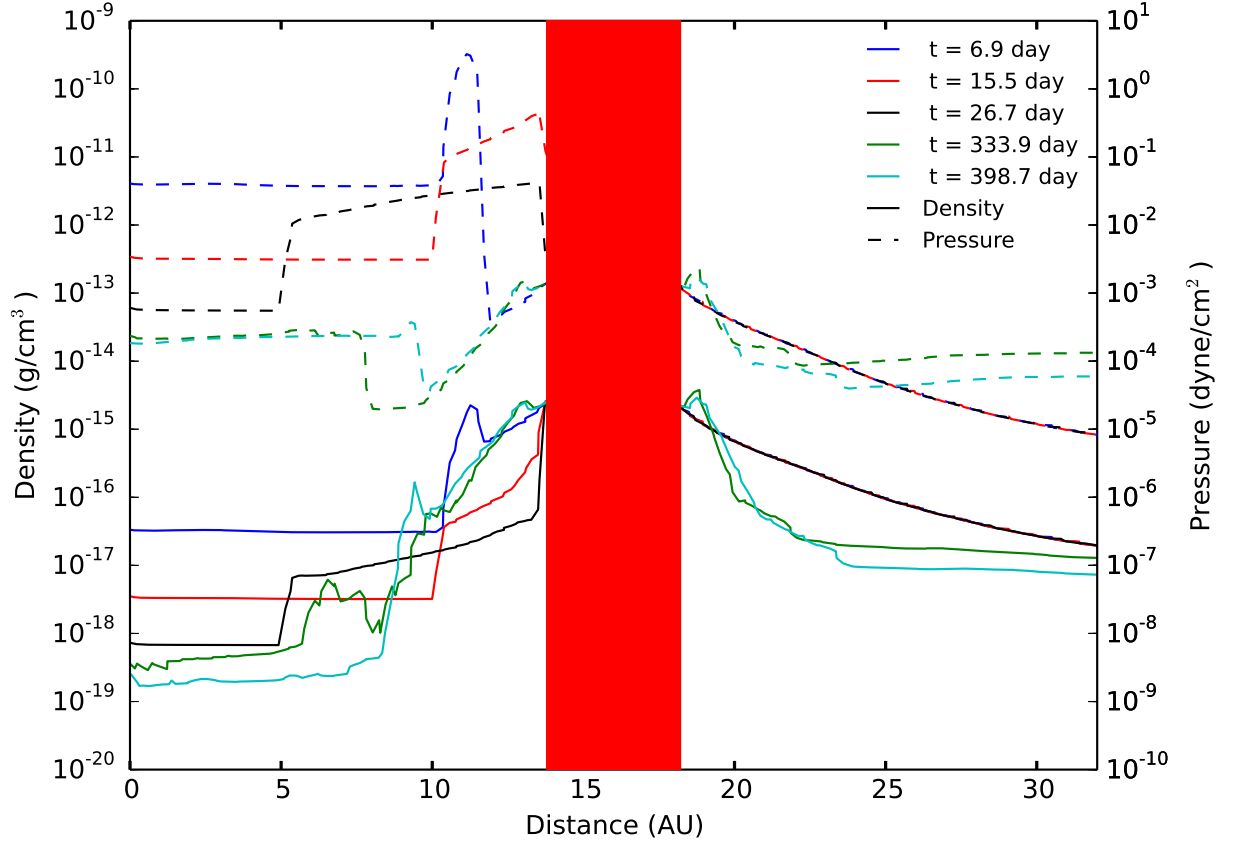


Fig. 10.— Density (solid lines) and pressure (dashed lines) profiles along the line extending from the WD to the RG for model M6E44. Different colors represent different times after the RN eruption. The red shaded region shows the location of the RG.

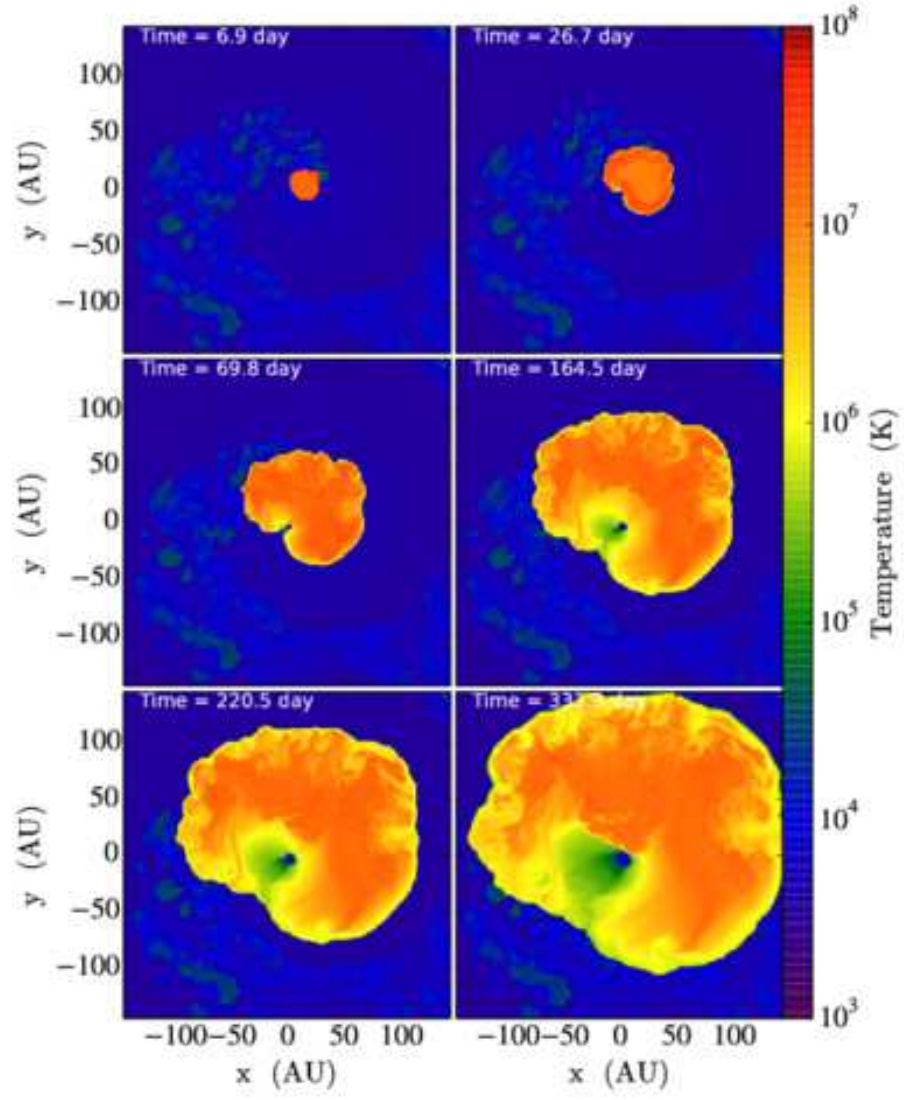


Fig. 11.— Similar to Figure 2 but for the eruption phase of model M6E44.

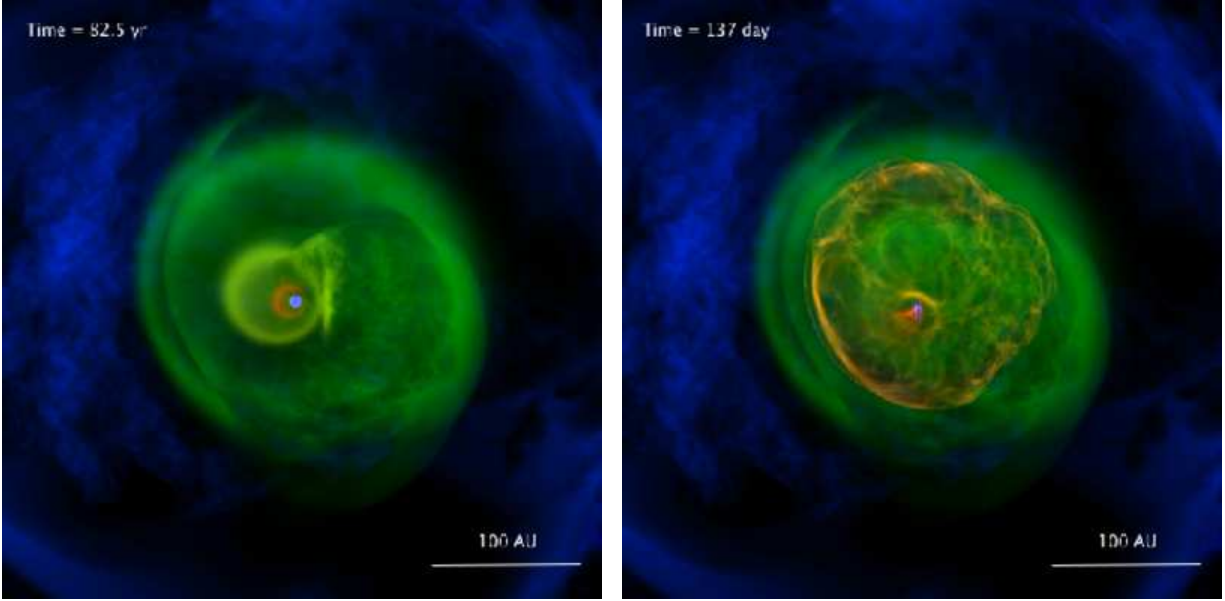


Fig. 12.— 3D volume rendering of gas density for models M6 and M6E44 at different simulation phases. Left: In the quiescent phase (model M6), the labeled time indicates the simulation time since the start of the simulation. Right: In the eruption phase (model M6E44), the labeled time indicates the simulation time after nova eruption. Orange colors in the right panel show the location of the nova shock. Red and yellow colors represent high-density regions; green and deep blue colors denote low-density regions. (movies of simulations are available online).

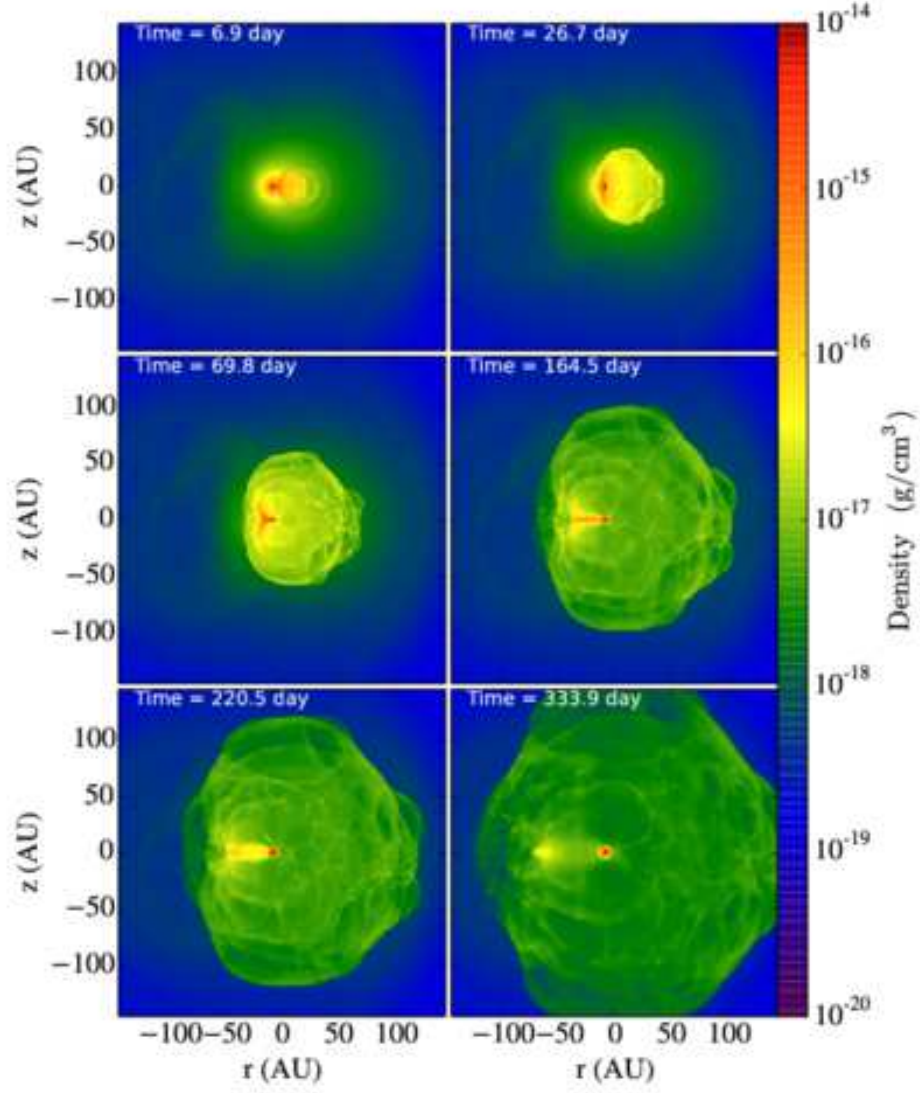


Fig. 13.— Similar to Figure 5 but for the eruption phase of model M6E44. The labeled times indicate the time after a nova eruption.

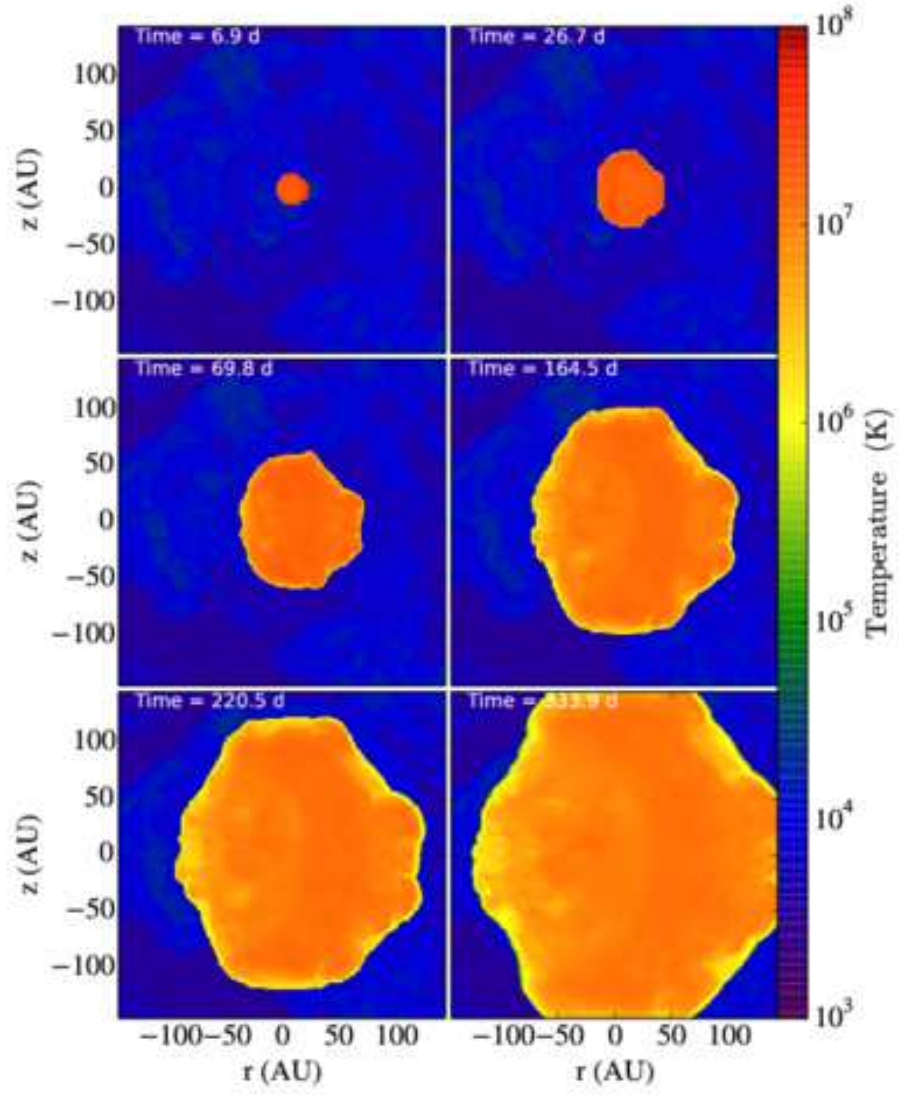


Fig. 14.— Similar to Figure 13 but gas temperature.

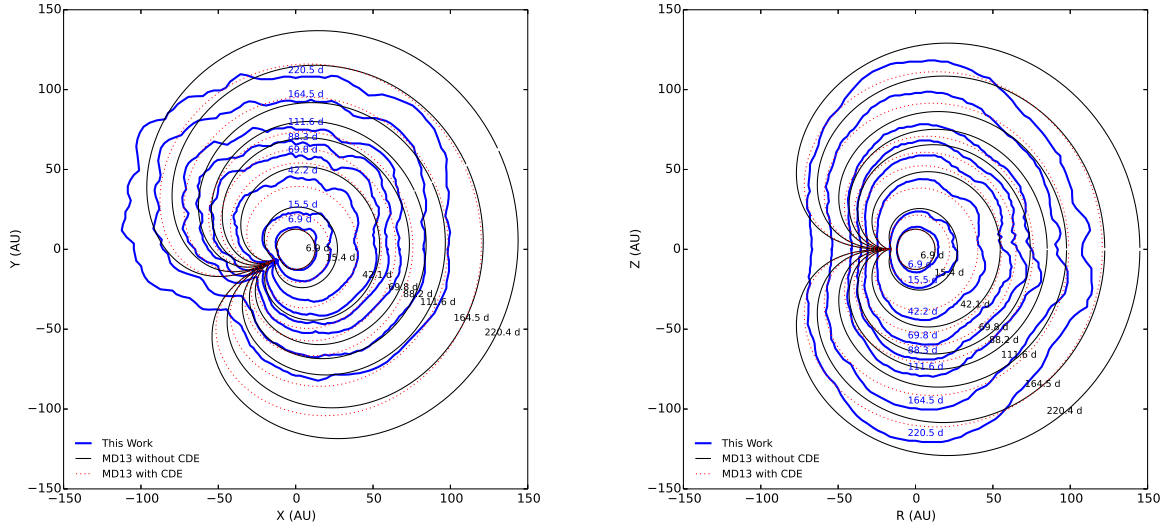


Fig. 15.— Shock radius evolution. Left: in the orbital plane. Right: in the $r - z$ plane perpendicular to the orbital plane. Blue contours indicate the shock radius evolution of model M6E44 at different times. Black contours show a comparison of shock radius evolution with a simple analytical model (denoted by the label MD13) by Martin & Dubus (2013). Red dots represent the same simple analytical model, but with the CDE.

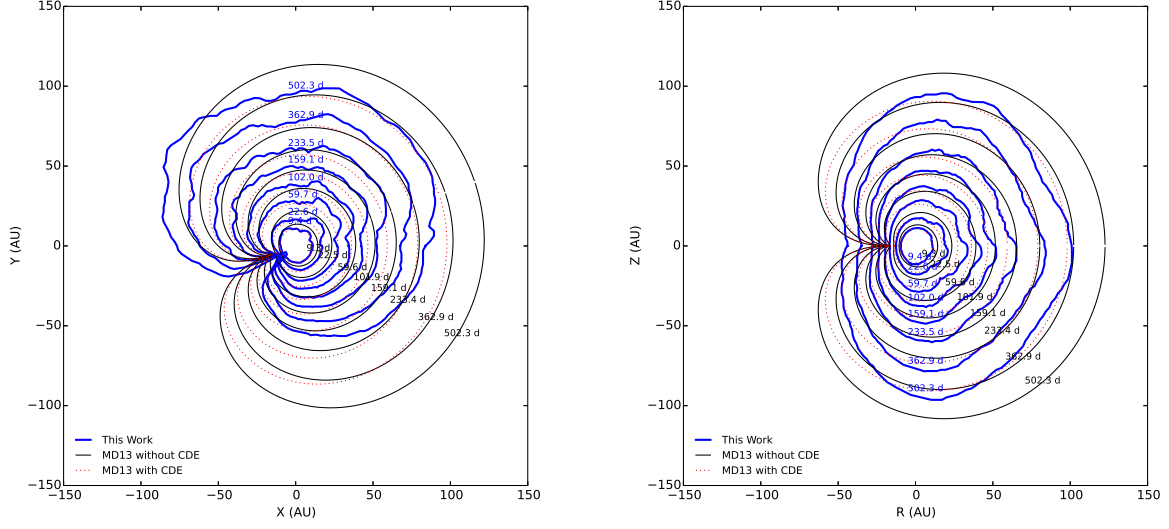


Fig. 16.— Similar to Figure 15 but for model M6E43.

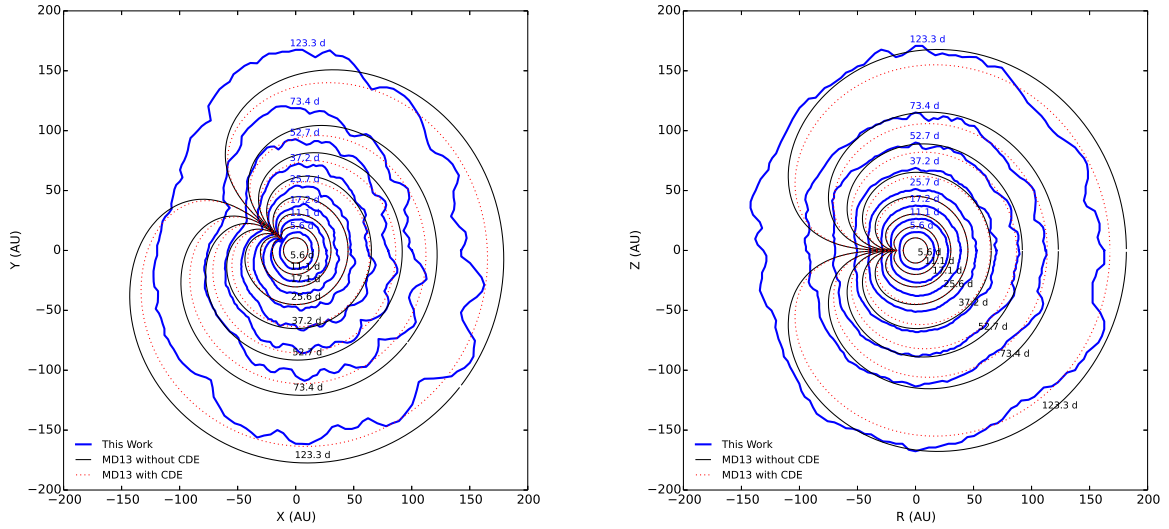


Fig. 17.— Similar to Figure 15 but for model M7E44.

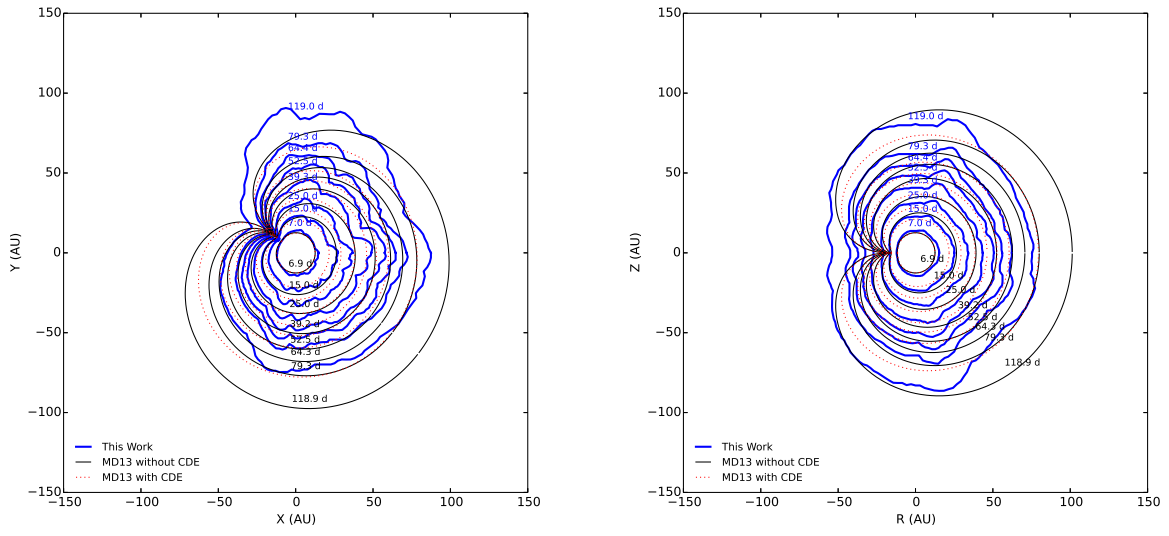


Fig. 18.— Similar to Figure 15 but for model M7E43.

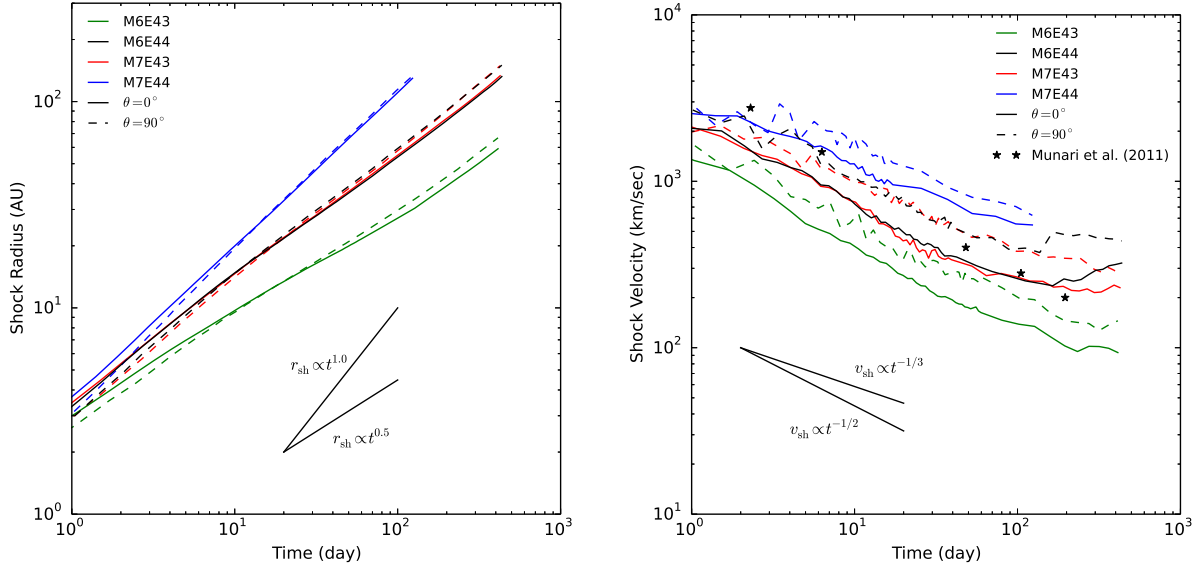


Fig. 19.— Time evolution of angle-averaged forward shock radius (left) and velocity (right). Different colors represent different eruption simulations in Table 1. Solid lines indicate the averaged shock radius (velocity) in the orbital plane. Dashed lines show averaged shock radius (velocity) in the poleward region. Star symbols represent the observed ejecta speed from Munari et al. (2011).